

Near-Field Wideband Localization using TTD-Based Terahertz Extremely Large-Scale Arrays

Qianyu Yang, *Member, IEEE*, Haiyang Zhang, *Member, IEEE*, Francesco Guidi, *Member, IEEE*, Anna Guerra, *Member, IEEE*, Davide Dardari, *Fellow, IEEE*, Baoyun Wang, *Senior Member, IEEE*, and Yonina C. Eldar, *Fellow, IEEE*

Abstract—The synergy between extremely large-scale antenna arrays and terahertz technology in sixth-generation networks establishes a near-field wideband transmission environment, enabling the generation of highly focused beams. To leverage this capability for multi-source localization, we propose a direct localization method based on the curvature-of-arrival of spherical wavefronts for estimating the positions of multiple near-field users from wideband signals. Furthermore, to overcome the spatial-wideband effect, we introduce a hybrid analog/digital array architecture with true-time-delayers (TTDs). We derive a closed-form position error bound to characterize the fundamental estimation performance and optimize the analog coefficients of array by maximizing the trace of the Fisher information matrix to minimize this bound. Furthermore, we extend this method to a sub-optimal iterative method that jointly optimizes beam focusing and localization, without requiring prior knowledge of the source positions for array design. Simulation results show that the proposed array configuration design significantly enhances the performance of near-field wideband localization, while the presence of TTDs effectively mitigates the localization performance degradation caused by spatial-wideband effects.

I. INTRODUCTION

In sixth generation (6G) networks, the integration of extremely large-scale antenna arrays (ELAAs) and the utilization of Terahertz (THz) bands are expected to notably enhance radio frequency (RF) positioning accuracy [1]. Specifically, THz wideband radio positioning is expected to undergo significant advancements and widespread adoption, as the wide bandwidth available will result in high spatial resolution, and the feasibility of large antenna arrays enables unprecedented angular resolution [2]–[4]. The transition towards ELAAs and the incorporation of THz frequency bands entail more than just an increase in bandwidth and the ability to stack more antenna elements on a given platform [5]–[7]. These advancements involve operating with fewer RF chains than elements and integrating analog processing to a certain extent in 6G networks [8]–[10]. They also bring

about substantial alterations in the electromagnetic characteristics of the wireless environment, transitioning from planar wave to spherical wave propagation, thereby signal transmission occurs within the radiating near-field region [1], [11].

Hybrid architectures, which utilize fewer RF chains than antenna elements, often employ phase shifter (PS) networks [12]–[14] to connect multiple antennas to less RF chains, forming arrays with high-dimensional analog processing and low-dimensional digital processing. However, in THz systems, the spatial-wideband effect leads to beam split, causing non-overlapping main lobes of the array gain corresponding to the lowest and highest subcarriers, resulting in a significant degradation of positioning estimation accuracy [15], [16]. Specifically, PSs are typically optimized for a single frequency (i.e., the central frequency), while in wideband systems, different frequencies across the band experience different phase shifts due to their varying wavelengths. Since phase shifters do not account for these variations across frequencies, the direction of the main beam “splits” or shifts off the intended target as the frequency moves away from the center. This shift creates an unintended offset in the beams direction, especially noticeable in systems with a large frequency range. While matrix projection techniques aim to alleviate this issue [17], their effectiveness is hampered by the frequency-independent nature of PSs [18].

To address this challenge, true-time delayers (TTDs) can be integrated into arrays to enable frequency-dependent beamforming. Specifically, the time delay introduced by TTDs induces frequency-dependent phase shifts across different subcarriers, thereby enabling distinct beamforming patterns to be applied to each subcarrier signal with different frequency and effectively mitigating the beam squint effect. Moreover, to manage the high power consumption and hardware complexity of TTDs, mainstream TTD-based hybrid arrays typically incorporate a limited number of TTDs between the PSs and RF chains [19]–[22]. For instance, [19] analyzed the array gain loss resulting from the beam splitting effect in THz massive MIMO systems and addressed the issue through the incorporation of TTDs. Meanwhile, [20] extended TTD-based wideband beamforming to the near-field scenario. Based on the conventional fully-connected TTD-based architecture, [21] considered practical maximum delay constraints of TTDs and proposed a hybrid serialparallel TTD configuration that relaxes the maximum delay requirements per TTD. Furthermore, [22] introduced a partially-connected TTD-based hybrid architecture aimed at improving energy efficiency and reducing the number of TTDs required. These studies demonstrate that these configurations can achieve near-optimal

Q. Yang is with the School of Information and Software Engineering, East China Jiaotong University, Nanchang 330013, China (e-mail: 3763@ecjtu.edu.cn). B. Wang is with the School of Communication and Information Engineering, Nanjing University of Posts and Telecommunications, Nanjing, China (e-mail: bywang@njupt.edu.cn). H. Zhang is with the School of Communication and Information Engineering, Nanjing University of Posts and Telecommunications. He is also with the National Mobile Communications Research Laboratory, Southeast University, Nanjing 210096, China (e-mail: haiyang.zhang@njupt.edu.cn). F. Guidi is with the National Research Council of Italy, IEIIT, Bologna, Italy (e-mail: francesco.guidi@cnr.it). A. Guerra and D. Dardari are with the Department of Electrical, Electronic, and Information Engineering Guglielmo Marconi - DEI-CNIT, University of Bologna, Cesena, Italy (e-mail: {anna.guerra3,davide.dardari}@unibo.it). Y. C. Eldar is with the Faculty of Math and CS, Weizmann Institute of Science, Rehovot, Israel (e-mail: yonina.eldar@weizmann.ac.il).

performance in terms of communication rates while minimizing power consumption. Nevertheless, the utilization of TTD-based hybrid architectures for wideband localization in the radiating near-field has been relatively overlooked in existing literature.

Differently from far-field localization scenarios [23], [24], in the radiating near-field, where wireless systems employing ELAAs at high frequency bands are expected to operate, the spherical shape of the wavefront becomes non-negligible [25]. Such wavefronts introduce new degrees of freedom that can be leveraged to enhance wireless localization, enabling direct and precise localization [26]–[32]. This method involves estimating positions, including distance and azimuth of users, directly from the curvature of the spherical wavefront, known as the curvature-of-arrival (COA) based localization technique [33]–[35]. Recent studies in the realm of 6G have considered COA-based localization, focusing on various aspects such as characterizing the Cramer-Rao bound (CRB) [33], exploring RIS-assisted configurations [34], and tracking methods [35]. Additionally, [36], [37] inquired near-field localization with hybrid arrays, showcasing the design of analog coefficients in hybrid arrays for near-field localization can achieve a form of beamfocusing. Similar findings were reported for integrated sensing and communications in [38], [39].

Most existing works of near-field wireless positioning focus on narrowband scenarios. However, with the advent of 6G technologies like ELAAs and THz technology systems, many applications operate in wideband near-field environments [22], which is far less studied compared to its narrowband counterparts. In particular, [40] investigated near-field processing for THz systems with a sparse transceiver array, but impact of the beam split was overlooked. The work [41] employed a noise subspace correction approach to address the beam split effect, yet it fails to mitigate the array gain loss stemming from this phenomenon. This motivates exploring wideband near-field multi-user localization using a TTD-based hybrid array.

In this work, we investigate RF positioning based on maximum likelihood (ML) estimation using wideband signals in the radiating near-field with a hybrid antenna array. To mitigate the beam split effect inherent in wideband systems, we employ hybrid arrays incorporating TTD units. Furthermore, we optimize the analog coefficients (i.e., the phase of PSs and the delay of TTDs) to enhance localization performance. Based on a novel problem formulation, we derive a closed-form expression for the CRB on ML position estimation. This derivation elucidates how the design of analog coefficients improves localization accuracy in wideband settings by maximizing the Fisher information matrix (FIM). Subsequently, we develop an iterative algorithm utilizing alternating optimization to simultaneously achieve beam focusing and user localization.

Our main contributions are summarized as follows:

- TTD-Based Wideband COA-Based Localization: We present a COA-based wideband localization method, designed to achieve simultaneous localization and beam focusing in the radiating near field with a TTDs-based hybrid array.
- Fundamental Localization Limits Analysis: We derive the CRB for the position estimates obtained via the proposed localization algorithm, which demonstrates the connection between the localization performance and the analog coefficients design. Subsequently, we formulate an

optimization problem for the design of analog coefficients to minimize the CRB, enhancing the effectiveness of the localization algorithm.

- Beamfocusing Algorithm: We employ an alternating optimization approach to reframe the analog coefficients coupling optimization problem into two separate sub-problems: one concerning the PSs coefficients and the other the TTDs coefficients. These sub-problems are solved individually based on assumed user positions, allowing us to iteratively converge on an approximate solution to the original problem. Subsequently, we expand our design to include a sub-optimal iterative method that eliminates the need for prior knowledge of user positions.
- Extensive Simulation Analysis: We conduct a comprehensive numerical analysis to showcase that the proposed solution notably boosts the performance of wideband near-field localization.

The rest of the paper is organized as follows: Section II describes the considered wideband signal model and antenna architecture. Section III formulates COA-based localization for a given beampattern, and analyzes its associated CRB. In Section IV, we formulate joint beamfocusing and localization as an optimization problem, based on which the proposed algorithm is derived. Subsequently, Section V reports the numerical results. Finally Section VI provides concluding remarks.

Notations: Scalar variables, vectors, and matrices are represented with lower letters, lower bold letters, and capital bold letters, respectively (e.g., x , \mathbf{x} , and \mathbf{X} , respectively). The term $\mathbb{C}^{N \times N}$ denotes a complex space of dimension $N \times N$, the superscripts $(\cdot)^T$ and $(\cdot)^H$ denote the transpose and Hermitian transpose, respectively, $|\cdot|$ is the absolute value operator, $\|\cdot\|$ is the Frobenius norm, $\text{blkdiag}(\mathbf{X}_1, \dots, \mathbf{X}_N)$ denotes a block diagonal matrix with diagonal blocks $\mathbf{X}_1, \dots, \mathbf{X}_N$, and $[\mathbf{x}]_n$ denotes the n -th elements of vector \mathbf{x} .

II. SYSTEM MODEL

In this section we present the considered wideband near-field localization system model. We first formulate the corresponding received signal model in Section II-A, and then introduce the considered array architectures in Section II-B.

A. Received Signal Model

We consider a multi-user localization scenario in which a base station receives pilot signals from K single-antenna users to estimate their locations. The base station comprises a uniform linear array (ULA) with N antenna elements separated by a distance Δ . In the uplink transmission, all users share the pilot spectrum, transmitting M Orthogonal Frequency-Division Multiplexing (OFDM) subcarriers within a bandwidth B at central carrier frequency f_c . Accordingly, the frequency of the m -th subcarrier with $m \in 1, \dots, M$, defined as f_m , is obtained from a uniform division of the frequency interval $[f_c - B/2, f_c + B/2]$. When communication takes place in traditional bands (e.g., sub 6 GHz), it is possible to uniformly process each subcarrier based on f_c . However, in highly wideband (e.g., THz) systems, the large bandwidth results in the beam splitting effect, and the frequency difference of each subcarrier cannot be ignored.

To formulate the resulting signal model, let $\mathbf{x}_m = [x_{m,1}, \dots, x_{m,n}, \dots, x_{m,N}]^T \in \mathbb{C}^N$ denote the received signal components of the m -th subcarrier at the base stations's array. Each source emits a standardized pilot signal with unit power. The signal received by the n -th antenna of the ULA at a specific discrete time instance can be expressed as:

$$x_{m,n} = \sum_{k=1}^K x_{m,k,n} + z_{m,n}. \quad (1)$$

In (1), $z_{m,n}$ is the additive white Gaussian noise at the n -th antenna for the m -th pilot symbol which has variance $\sigma_{m,n}^2$, and $x_{m,k,n}$ is the received signal of the m -th subcarrier from the k -th user at the corresponding antenna. The latter can be expressed as

$$x_{m,k,n} = g_{m,k,n} c_k, \quad (2)$$

where c_k is the data symbol corresponding to the k -th user, which satisfies $\mathbb{E}\{|c_k|^2\} = 1$, and $g_{m,k,n} = \alpha_{m,k} e^{-jv_{m,k,n}}$ represents the channel component, with $\alpha_{m,k}$ and $v_{m,k,n}$ denoting the channel gain coefficient and the phase due to the distance traveled by the signal, respectively. The gain is expressed as $\alpha_{m,k} = \frac{c}{4\pi f_m d_k}$ with d_k indicating the distance between the array and the user¹, and the phase is given by

$$v_{m,k,n} \triangleq 2\pi f_m \frac{d_{k,n}}{c}. \quad (3)$$

In (3), $d_{k,n}$ is the distance between the corresponding antenna and the user, and c is the speed of light. Consequently, \mathbf{x}_m can be written as

$$\mathbf{x}_m = \sum_{k=1}^K \mathbf{g}_{m,k} c_k + \mathbf{z}_m = \mathbf{G}_m \mathbf{c} + \mathbf{z}_m, \quad (4)$$

where $\mathbf{g}_{m,k} = [g_{m,k,1}, \dots, g_{m,k,n}, \dots, g_{m,k,N}]^T \in \mathbb{C}^{N \times 1}$ and $\mathbf{z}_m = [z_{m,1}, \dots, z_{m,n}, \dots, z_{m,N}]^T \in \mathbb{C}^{N \times 1}$ denote the channel vector and noise vector, respectively. The matrix $\mathbf{G}_m = [\mathbf{g}_{m,1}, \dots, \mathbf{g}_{m,K}] \in \mathbb{C}^{N \times K}$ is the channel matrix, and $\mathbf{c} = [c_1, \dots, c_K]^T \in \mathbb{C}^{K \times 1}$ denotes the symbol vector.

B. Array Architecture

The antenna array utilized by the base station is based on a hybrid architecture, being a widely adopted technique for realizing large scale antennas at high frequencies in an affordable manner [10]. We specifically consider TTD-based hybrid array configurations, in which large number of antenna elements is connected to a smaller number of RF chains through dedicated analog circuitry comprised of TTD units, as depicted in Fig. 1. In this architecture, TTD-based preprocessing of the received signal achieves frequency-independent phase adjustment. This TTD-based hybrid array setup employs N_d RF chains to connect to N antennas utilizing a restricted level of analog signal processing, each antenna connects to an RF chain via an individual PS and a shared TTD [22].

Specifically, the array is partitioned into several linear sub-arrays, each comprising N_s elements arranged uniformly. Each linear sub-array is managed by a fully interconnected PS network

with a TTD. Subsequently, the TTDs are divided into N_d groups, each containing N_t TTDs, with each group linked to an RF chain. Consequently, the array incorporates $N_t N_s$ TTDs and N PSs, satisfying the condition $N = N_d N_t N_s$. The signal of the m -th subcarrier $\mathbf{y}_m = [y_{m,1}, \dots, y_{m,i}, \dots, y_{m,N_d}]^T \in \mathbb{C}^{N_d \times 1}$, which is processed in digital after analog combination, is thus given by

$$\mathbf{y}_m = \mathbf{Q}_m \mathbf{x}_m, \quad (5)$$

where \mathbf{Q}_m is the analog combination matrix, which is determined jointly by the TTDs and PSs as

$$\mathbf{Q}_m = \mathbf{T}_m \mathbf{A}. \quad (6)$$

In (6), $\mathbf{T}_m \in \mathbb{C}^{N_d \times N_d N_t}$ and $\mathbf{A} \in \mathbb{C}^{N_d N_t \times N}$ represent the analog processing carried out by the TTDs and PSs, which are given by

$$\mathbf{T}_m = \text{blkdiag}(e^{j2\pi f_m \mathbf{t}_1}, \dots, e^{j2\pi f_m \mathbf{t}_{N_d}}), \quad (7)$$

$$\mathbf{A} = \text{blkdiag}(\mathbf{a}_{1,1}, \dots, \mathbf{a}_{i,l}, \dots, \mathbf{a}_{N_d, N_t}), \quad (8)$$

respectively. In (7) $\mathbf{t}_i = [t_{i,1}, \dots, t_{i,N_t}] \in \mathbb{C}^{N_t}$ is the time delay vector of TTDs at the i -th RF chain, with $t_{i,l} \in [0, t_{\max}]$, $i \in \{1, \dots, N_d\}$, $l \in \{1, \dots, N_t\}$, here t_{\max} being the maximum delay of each TTD. In (8), $\mathbf{a}_{i,l} \in \mathbb{C}^{N_s}$ is the PS coefficient vector connect to the l -th TTD at the i -th RF chain, its internal element a_n denotes the coefficient of the PS corresponding to the n -th antenna with $n \in \mathcal{N}_{i,l} = \{(i-1)N_t + l - 1, \dots, (i-1)N_t + l\}$, which is frequency independent and given by

$$a_n \in \mathcal{F} \triangleq \{e^{j\phi_n} \mid \phi_n \in [0, 2\pi]\}. \quad (9)$$

Hence, the entries of the digital input (5) can be expressed as

$$y_{m,i} = \sum_{l=1}^{N_t} e^{j2\pi f_m t_{i,l}} \sum_{n \in \mathcal{N}_{i,l}} a_n x_{m,n}. \quad (10)$$

Our objective is to estimate user positions based on received wideband signal observations $\{\mathbf{y}_m\}_{m=1}^M$. As evident from (5) and (10), the considered array architecture facilitates distinct analog combinations for each received signal \mathbf{y}_m . Therefore, by adjusting the combinations constrained by (7) and (8), the received signal will be subjected to frequency dependent modulation to avoid beam splitting.

III. LOCALIZATION WITH FIXED ANALOG COMBINATION

The array architecture modeling in (10) indicates that one can affect the signal processed in digital (and used for localization) by manipulating the analog configuration \mathbf{Q}_m , represented by \mathbf{T}_m and \mathbf{A} . To understand how the setting of these analog combining parameters affect the ability to localize multiple users based on wideband transmission, we start by studying localization for a fixed analog combiner and analyze the associated CRB of estimation result. To that aim, we first characterize a suitable localization algorithm based on the maximum likelihood rule before the CRB analysis.

A. Maximum Likelihood Localization

1) *Localization Setting*: The utilization of the radiating near-field in communication can be leveraged to enhance localization

¹Here we neglect the near-field model of amplitudes, as above variation in channel gain between different antennas of the array is small enough [42].

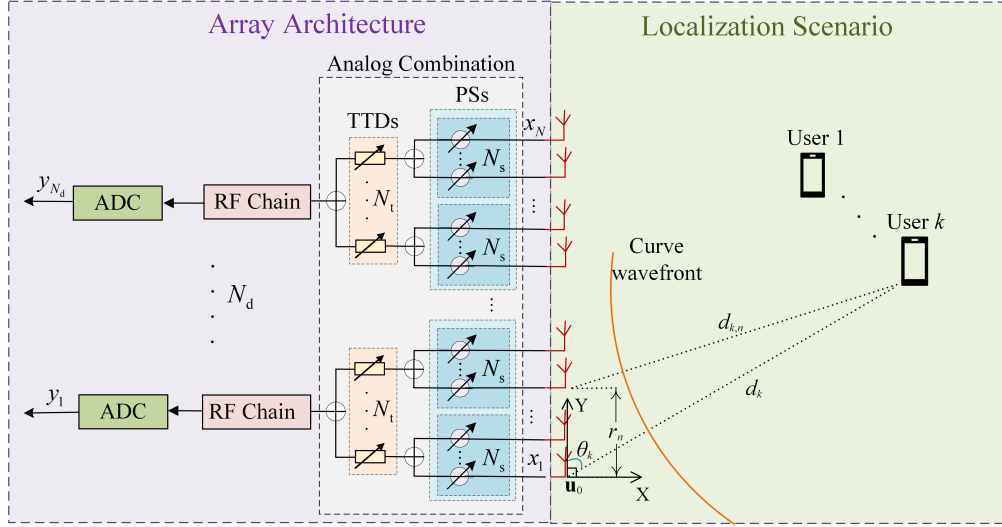


Fig. 1. System model diagram. Left diagram: the array architectures; Right diagram: the localization scenario.

through the COA estimation of the impinging signal at different antennas. The localization scenario under consideration, depicted in Fig. 1, establishes a reference point (an antenna) \mathbf{u}_0 situated at $(0, 0)$ within the receiving array. The ULA is oriented along the Y -axis, with the k -th user positioned at (x_k, y_k) , a distance of d_k , and an azimuth angle θ_k relative to the source (refer to Fig. 1). Moreover, the n -th antenna of the array is positioned at $(0, r_n)$ with respect to the array's reference point, where $r_n = (N - 1)\Delta$. The specific geometric relationships between coordinates and reference positions can be described as:

$$x_k = d_k \cos \theta_k, \quad y_k = d_k \sin \theta_k. \quad (11)$$

According to the triangular relationship, the distance of the k th user from the n th antenna can be expressed as [35]

$$d_{k,n}(d_k, \theta_k) = \sqrt{r_n^2 + d_k^2 - 2r_n d_k \cos \theta_k}. \quad (12)$$

2) *Maximum Likelihood Formulation:* The formulation (12) establishes the intricate link between the user's location and the phase distribution, preserving the nonlinearity within the aforementioned output. Hence, one viable approach for user position estimation involves the computation of the maximum likelihood estimation (MLE). By consolidating the received signals across M sub-frequencies, we have $\mathbf{y} = [\mathbf{y}_1^T, \dots, \mathbf{y}_M^T]^T$, which we express as

$$\mathbf{y} = \mathbf{Q}\mathbf{G}\hat{\mathbf{c}} + \mathbf{Q}\mathbf{z}, \quad (13)$$

where $\hat{\mathbf{c}} = \mathbf{I}_M \otimes \mathbf{c} \in \mathbb{C}^{MK \times 1}$, $\mathbf{z} = [\mathbf{z}_1^T, \dots, \mathbf{z}_M^T]^T$, $\mathbf{Q} = \text{blkdiag}(\mathbf{Q}_1, \dots, \mathbf{Q}_M)$, $\mathbf{G} = \text{blkdiag}(\mathbf{G}_1, \dots, \mathbf{G}_M)$. According to (7) and (8), we have $\mathbf{Q}_m \mathbf{Q}_m^T = N_t N_s \mathbf{I}_{N_d}, \forall m$.

We define the unknown parameters vector to be estimated from (13) as $\boldsymbol{\eta} = [\mathbf{d}, \boldsymbol{\theta}] \in \mathbb{C}^{2K}$, with $\mathbf{d} = [d_1, \dots, d_K]$ and $\boldsymbol{\theta} = [\theta_1, \dots, \theta_K]$ refer to the possible user positions set in polar coordinates, respectively. The position MLE is given by

$$\hat{\boldsymbol{\eta}} = \arg \max_{\boldsymbol{\eta}} \log p(\mathbf{y}; \boldsymbol{\eta}, \mathbf{Q}), \quad (14)$$

where $\log p(\mathbf{y}; \boldsymbol{\eta}, \mathbf{Q})$ is the log-likelihood function of \mathbf{y} .

The MLE process is based on an observation time window consisting of L samples. The l -th sample is denoted as $\mathbf{y}(l)$ for $l = 1, \dots, L$. Given (13), once a sufficient quantity of receiving samples is obtained, the log-likelihood function of \mathbf{y} can be articulated as [43]

$$\begin{aligned} \log p(\mathbf{y}; \boldsymbol{\eta}, \mathbf{Q}) &= \log p(\mathbf{y}_1, \dots, \mathbf{y}_M; \boldsymbol{\eta}, \mathbf{Q}) \\ &\propto \sum_{l=1}^L \sum_{m=1}^M \|\mathcal{P}[\mathbf{S}_m(\boldsymbol{\eta}, \mathbf{Q})] \mathbf{y}_m(l)\|^2 \\ &\propto \sum_{m=1}^M \text{tr}[\mathcal{P}[\mathbf{S}_m(\boldsymbol{\eta}, \mathbf{Q})] \mathbf{R}_m], \end{aligned} \quad (15)$$

where \mathbf{R}_m is the empirical average of $\mathbf{y}_m \mathbf{y}_m^H$ over the observed time window, and \mathcal{P} denotes the projection operator, which, when applied to a matrix \mathbf{X} , is given by

$$\mathcal{P}[\mathbf{X}] = \mathbf{X} [\mathbf{X}^H \mathbf{X}]^{-1} \mathbf{X}^H.$$

Projection in (15) is applied to $\mathbf{S}_m(\boldsymbol{\eta}, \mathbf{Q}) = \mathbf{Q}_m \mathbf{S}_m^d(\boldsymbol{\eta})$, and $\mathbf{S}_m^d(\boldsymbol{\eta}) = [\mathbf{s}_{m,1}^d(\boldsymbol{\eta}_1), \dots, \mathbf{s}_{m,K}^d(\boldsymbol{\eta}_K)] \in \mathbb{C}^{N \times M}$ is the steering matrix of the array with

$$\mathbf{s}_{m,k}^d(\boldsymbol{\eta}_k) = \alpha_{m,k} \left[e^{-jv_{m,k,1}(\boldsymbol{\eta}_k)}, \dots, e^{-jv_{m,k,N}(\boldsymbol{\eta}_k)} \right]^T, \quad (16)$$

where $\boldsymbol{\eta}_k = [d_k, \theta_k]$, and $v_{m,i,l}(\boldsymbol{\eta}_k)$ is obtained from (3) and (12) thus determined by $\boldsymbol{\eta}_k$.

3) *MLE Computation via Alternating Projection:* Problem (15) can be solved by the alternating projection (AP) method to avoid the complexity of the multi-dimensional maximization problem [37]. Specifically, we define the vector $\boldsymbol{\eta}_{-k} = [\mathbf{d}_{-k}, \boldsymbol{\theta}_{-k}] \in \mathbb{C}^{2K-2}$, where $\mathbf{d}_{-k} = [d_1, \dots, d_{k-1}, d_{k+1}, \dots, d_K]$ and $\boldsymbol{\theta}_{-k} = [\theta_1, \dots, \theta_{k-1}, \theta_{k+1}, \dots, \theta_K]$, then the projection operator $\mathcal{P}[\mathbf{S}_m(\boldsymbol{\eta}, \mathbf{Q})]$ can be rewritten as

$$\mathcal{P}[\mathbf{S}_m(\boldsymbol{\eta}, \mathbf{Q})] = \mathcal{P}[\mathbf{S}_m(\boldsymbol{\eta}_{-k}, \mathbf{Q})] + \mathcal{P}[\bar{\mathbf{s}}_m(\boldsymbol{\eta}_k, \mathbf{Q})], \quad (17)$$

where $\mathbf{S}_m(\boldsymbol{\eta}_{-k}, \mathbf{Q}) \in \mathbb{C}^{N_d \times K-1}$ is the steering matrix based on $\boldsymbol{\eta}_{-k}$ and \mathbf{Q} , and $\bar{\mathbf{s}}_m(\boldsymbol{\eta}_k, \mathbf{Q})$ is given by

$$\bar{\mathbf{s}}_m(\boldsymbol{\eta}_k, \mathbf{Q}) = (\mathbf{I}_{N_d} - \mathcal{P}[\mathbf{S}(\boldsymbol{\eta}_{-k}, \mathbf{Q})]) \mathbf{Q}_m \mathbf{s}_{m,k}^d(\boldsymbol{\eta}_k), \quad (18)$$

which denotes the residual of $\mathbf{Q}_m \mathbf{s}_{m,k}^d$ when projected on $\mathbf{S}_m(\boldsymbol{\eta}_{-k}, \mathbf{Q})$

From (17), for a given analog configuration \mathbf{Q} , once $\boldsymbol{\eta}_{-k}$ has been fixed, $\mathcal{P}[\mathbf{S}_m(\boldsymbol{\eta}, \mathbf{Q})]$ becomes solely reliant on $\boldsymbol{\eta}_k$. Consequently, the maximization of (15) can be addressed alternating iteratively with each iteration involving the maximization concerning a single parameter $\boldsymbol{\eta}_k$ while keeping all other parameters constant. Thus, by substituting (17) into (15), the problem posed in (14) can be streamlined into solving M sub-problems, where the m -th sub-problem is formulated as:

$$\begin{aligned} \boldsymbol{\eta}_k &= \arg \max_{\boldsymbol{\eta}_k} \log p(\mathbf{y}; \boldsymbol{\eta}_k, \mathbf{Q}) \\ &\propto \sum_{m=1}^M \text{tr}[\mathcal{P}[\bar{\mathbf{s}}_m(\boldsymbol{\eta}_k, \mathbf{Q})] \mathbf{R}_m] \end{aligned} \quad (19)$$

One can calculate (19) when \mathbf{Q} is held constant, with the detailed process summarized as Algorithm 1. The initial estimation begins with a single-user scenario to determine the position of the first user. Subsequently, the algorithm fixes the existing estimates and progressively incorporates additional users until reaching the final estimation. This incremental approach aids in refining the localization process step by step. We note that the proposed Algorithm 1 is also applicable to narrowband system. In narrowband system case, all subcarriers would be tuned by a unified phase shift from PSs without TTDs, that \mathbf{Q} would be given by $\mathbf{Q} = \text{blkdiag}(\mathbf{Q}_0, \dots, \mathbf{Q}_0)$, where \mathbf{Q}_0 is obtained from (6) with $t_{\max} = 0$.

Algorithm 1 AP-based wideband near-field localization.

Initialize: Set $t = 1$; The maximal number of iteration K_t ;

$\boldsymbol{\eta} \in \mathbb{R}^{2K}$, and $\mathcal{P}[\mathbf{S}_m(\boldsymbol{\eta}, \mathbf{Q})] = \mathbf{0}, \forall m$.

For $k = 1 : K$

1: For all m , calculate:

$\bar{\mathbf{s}}_m(\boldsymbol{\eta}_k, \mathbf{Q}) = (\mathbf{I}_{N_d} - \mathcal{P}[\mathbf{S}_m(\boldsymbol{\eta}, \mathbf{Q})]) \mathbf{Q}_m \mathbf{s}_{m,k}^d(\boldsymbol{\eta}_k)$.

2: Obtain $\boldsymbol{\eta}_k^0$ by solving (19) with calculated $\bar{\mathbf{s}}_m(\boldsymbol{\eta}_k, \mathbf{Q})$.

3: $\mathcal{P}[\mathbf{S}_m(\boldsymbol{\eta}, \mathbf{Q})] = \mathcal{P}[\mathbf{S}_m(\boldsymbol{\eta}, \mathbf{Q})] + \mathcal{P}[\bar{\mathbf{s}}_m(\boldsymbol{\eta}_k, \mathbf{Q})]$.

4: Initialize position set: $[\boldsymbol{\eta}]_k = [\boldsymbol{\eta}_{k1}^0]$, $[\boldsymbol{\eta}]_{K+k} = [\boldsymbol{\eta}_{k2}^0]$.

End

While $t \leq K_t$ **do**

For $k = 1 : K$

5: Obtain $\mathcal{P}[\bar{\mathbf{s}}_m(\boldsymbol{\eta}_k, \mathbf{Q})]$ from $\bar{\mathbf{s}}_m(\boldsymbol{\eta}_k, \mathbf{Q})$ as (18), $\forall m$.

6: Obtain $\boldsymbol{\eta}_k^t$ by solving (19) with calculated $\bar{\mathbf{s}}_m(\boldsymbol{\eta}_k, \mathbf{Q})$.

7: Update position set: $[\boldsymbol{\eta}]_k = [\boldsymbol{\eta}_{k1}^t]$, $[\boldsymbol{\eta}]_{K+k} = [\boldsymbol{\eta}_{k2}^t]$.

8: Update $\mathcal{P}[\mathbf{S}_m(\boldsymbol{\eta}, \mathbf{Q})] = \mathcal{P}[\mathbf{S}_m(\boldsymbol{\eta}, \mathbf{Q})] + \mathcal{P}[\bar{\mathbf{s}}_m(\boldsymbol{\eta}_k, \mathbf{Q})]$.

End

9: $t = t + 1$.

End while

Output: The estimated unknown parameters $\boldsymbol{\eta}$.

The computation of Algorithm 1 requires a given \mathbf{Q} . Therefore, the fact that the accuracy of this estimate depends on \mathbf{Q} allows us to use the above MLE as guidelines for the analog design along with the localization task.

B. Cramer-Rao Bound Analysis

The CRB serves as a fundamental lower limit on the variance of any unbiased estimator [44]. The CRB expression derived provides valuable insights into how system parameters and configurations, such as the analog combination, influence the performance of position estimation. For the likelihood model in (15), the array output \mathbf{y} can be regarded as a distribution with the mean vector $\boldsymbol{\mu}$ and covariance matrix $\boldsymbol{\Xi} = \text{blkdiag}(\sigma_1^2 N_t N_s \mathbf{I}_{MN_d}, \dots, \sigma_M^2 N_t N_s \mathbf{I}_{MN_d})$, where

$$\boldsymbol{\mu} = \mathbf{Q} \mathbf{S}^d(\boldsymbol{\eta}, \mathbf{Q}) \hat{\mathbf{c}}, \quad (20)$$

and $\mathbf{S}^d(\boldsymbol{\eta}, \mathbf{Q}) = \text{blkdiag}(\mathbf{S}_1^d(\boldsymbol{\eta}, \mathbf{Q}), \dots, \mathbf{S}_M^d(\boldsymbol{\eta}, \mathbf{Q}))$.

Let \mathbf{F} denotes the Fisher information matrix (FIM) for estimating parameter $\boldsymbol{\eta}$ from the data. The elements of the FIM are given by [45]

$$\begin{aligned} [\mathbf{F}]_{i,j} &= 2\mathcal{R} \left\{ \frac{\partial \boldsymbol{\mu}^H}{\partial [\boldsymbol{\eta}]_i} \boldsymbol{\Xi}^{-1} \frac{\partial \boldsymbol{\mu}}{\partial [\boldsymbol{\eta}]_j} \right\} + \text{tr} \left(\boldsymbol{\Xi}^{-1} \frac{\partial \boldsymbol{\Xi}}{\partial [\boldsymbol{\eta}]_i} \boldsymbol{\Xi}^{-1} \frac{\partial \boldsymbol{\Xi}}{\partial [\boldsymbol{\eta}]_j} \right) \\ &= 2\mathcal{R} \left\{ \frac{\partial \boldsymbol{\mu}^H}{\partial [\boldsymbol{\eta}]_i} \boldsymbol{\Xi}^{-1} \frac{\partial \boldsymbol{\mu}}{\partial [\boldsymbol{\eta}]_j} \right\}, \end{aligned} \quad (21)$$

where $[\boldsymbol{\eta}]_i$ denotes the i -th element of $\boldsymbol{\eta}$. According to (20) and the definition of \mathbf{Q} , we have the first-order derivative

$$\begin{aligned} \frac{\partial \boldsymbol{\mu}}{\partial \mathbf{d}} &= \mathbf{Q} \frac{\partial \mathbf{S}^d(\boldsymbol{\eta}, \mathbf{Q})}{\partial \mathbf{d}} \hat{\mathbf{c}} \\ &= [\mathbf{C} \mathbf{D}_1^T \mathbf{Q}_1^T, \dots, \mathbf{C} \mathbf{D}_M^T \mathbf{Q}_M^T]^T, \end{aligned} \quad (22)$$

$$\begin{aligned} \frac{\partial \boldsymbol{\mu}}{\partial \boldsymbol{\theta}} &= \mathbf{Q} \frac{\partial \mathbf{S}^d(\boldsymbol{\eta}, \mathbf{Q})}{\partial \boldsymbol{\theta}} \hat{\mathbf{c}} \\ &= [\mathbf{C} \mathbf{B}_1^T \mathbf{Q}_1^T, \dots, \mathbf{C} \mathbf{B}_M^T \mathbf{Q}_M^T]^T. \end{aligned} \quad (23)$$

Here $\mathbf{C} = \text{diag}(\mathbf{c})$, \mathbf{D}_m and \mathbf{B}_m are respectively defined as

$$\mathbf{D}_m = \left[\frac{\partial \mathbf{s}_{m,1}^d(\boldsymbol{\eta}_1)}{\partial d_1}, \dots, \frac{\partial \mathbf{s}_{m,K}^d(\boldsymbol{\eta}_K)}{\partial d_K} \right] \in \mathbb{C}^{N \times K}, \quad (24)$$

$$\mathbf{B}_m = \left[\frac{\partial \mathbf{s}_{m,1}^d(\boldsymbol{\eta}_1)}{\partial \theta_1}, \dots, \frac{\partial \mathbf{s}_{m,K}^d(\boldsymbol{\eta}_K)}{\partial \theta_K} \right] \in \mathbb{C}^{N \times K}. \quad (25)$$

The elements of the matrix in (24) and (25) are given by

$$\begin{aligned} [\mathbf{D}_m]_{n,k} &= \frac{\partial s_{m,k,n}^d}{\partial d_k} \\ &= -e^{-jv_{m,k,n}} \left(\frac{c}{4\pi f_m d_k^2} + \frac{j(d_k - r_n \cos \theta_k)}{2d_k d_{k,n}} \right), \end{aligned} \quad (26)$$

$$\begin{aligned} [\mathbf{B}_m]_{n,k} &= \frac{\partial s_{m,k,n}^d}{\partial \theta_k} \\ &= -e^{-jv_{m,k,n}} \frac{j r_n \sin \theta_k}{2d_{k,n}}. \end{aligned} \quad (27)$$

Then, according to the division of $\boldsymbol{\eta}$, the FIM can be represented as

$$\mathbf{F} = \begin{bmatrix} \mathbf{F}_{\mathbf{d}\mathbf{d}} & \mathbf{F}_{\mathbf{d}\boldsymbol{\theta}} \\ \mathbf{F}_{\boldsymbol{\theta}\mathbf{d}} & \mathbf{F}_{\boldsymbol{\theta}\boldsymbol{\theta}} \end{bmatrix}, \quad (28)$$

where each block matrix in (28) can be calculated separately as

$$\begin{aligned} \mathbf{F}_{\mathbf{d}\mathbf{d}} &= 2\mathcal{R} \left\{ \frac{\partial \boldsymbol{\mu}^H}{\partial \mathbf{d}^T} \boldsymbol{\Xi}^{-1} \frac{\partial \boldsymbol{\mu}}{\partial \mathbf{d}} \right\} \\ &= \frac{2}{N_t N_s} \sum_{m=1}^M \frac{1}{\sigma_m^2} \mathcal{R} \{ \mathbf{C}^H \mathbf{D}_m^H \mathbf{Q}_m^H \mathbf{Q}_m \mathbf{D}_m \mathbf{C} \}, \end{aligned} \quad (29)$$

$$\begin{aligned} \mathbf{F}_{\mathbf{d}\boldsymbol{\theta}} &= 2\mathcal{R} \left\{ \frac{\partial \boldsymbol{\mu}^H}{\partial \mathbf{d}^T} \boldsymbol{\Xi}^{-1} \frac{\partial \boldsymbol{\mu}}{\partial \boldsymbol{\theta}} \right\} \\ &= \frac{2}{N_t N_s} \sum_{m=1}^M \frac{1}{\sigma_m^2} \mathcal{R} \{ \mathbf{C}^H \mathbf{D}_m^H \mathbf{Q}_m^H \mathbf{Q}_m \mathbf{B}_m \mathbf{C} \}, \end{aligned} \quad (30)$$

$$\begin{aligned} \mathbf{F}_{\boldsymbol{\theta}\mathbf{d}} &= 2\mathcal{R} \left\{ \frac{\partial \boldsymbol{\mu}^H}{\partial \boldsymbol{\theta}^T} \boldsymbol{\Xi}^{-1} \frac{\partial \boldsymbol{\mu}}{\partial \mathbf{d}} \right\} \\ &= \frac{2}{N_t N_s} \sum_{m=1}^M \frac{1}{\sigma_m^2} \mathcal{R} \{ \mathbf{C}^H \mathbf{B}_m^H \mathbf{Q}_m^H \mathbf{Q}_m \mathbf{D}_m \mathbf{C} \}, \end{aligned} \quad (31)$$

$$\begin{aligned} \mathbf{F}_{\boldsymbol{\theta}\boldsymbol{\theta}} &= 2\mathcal{R} \left\{ \frac{\partial \boldsymbol{\mu}^H}{\partial \boldsymbol{\theta}^T} \boldsymbol{\Xi}^{-1} \frac{\partial \boldsymbol{\mu}}{\partial \boldsymbol{\theta}} \right\} \\ &= \frac{2}{N_t N_s} \sum_{m=1}^M \frac{1}{\sigma_m^2} \mathcal{R} \{ \mathbf{C}^H \mathbf{B}_m^H \mathbf{Q}_m^H \mathbf{Q}_m \mathbf{B}_m \mathbf{C} \}, \end{aligned} \quad (32)$$

To convert the estimation results from polar coordinates to Euclidean coordinates, we define the position parameter vector $\mathbf{p} = [x_1, \dots, x_K, y_1, \dots, y_K]$. Its corresponding FIM defined as $\mathbf{F}_{\mathbf{E}}$ is obtained by using the chain rule:

$$\mathbf{F}_{\mathbf{E}} = \mathbf{J}\mathbf{F}\mathbf{J}^T, \quad (33)$$

with $\mathbf{J} = \frac{\partial \boldsymbol{\eta}}{\partial \mathbf{p}^T} \in \mathbb{C}^{2K \times 2K}$ denoting the Jacobian matrix, which can be computed based on the relationship specified in (11). The CRB is given by the inverse of $\mathbf{F}_{\mathbf{E}}$, formulated as:

$$\text{CRB} = \sqrt{\text{tr}(\mathbf{F}_{\mathbf{E}}^{-1})}. \quad (34)$$

C. Discussion

Once \mathbf{Q} is given, the position error bound (PEB) of the estimated position \mathbf{p} can be given by the CRB expression in (34). This relationship motivates further investigation into how analog design influences localization performance. Although (34) provides a closed-form expression for the PEB, it does not explicitly reveal the dependence of localization accuracy on analog design. Instead, as (33) and (34), the structure of the FIMs in (29)-(32) explicitly demonstrates which factors affect the localization performance. Specifically, we will explore the factors that affect maximizing the trace of the FIMs, in order to achieve the minimization of CRB.

Firstly, each block matrix of the FIM can be decomposed into a superposition of M submatrices corresponding to different subcarrier components. This decomposition implies that wideband transmission with richer spectral resources can enhance localization accuracy by reducing the CRB. Specifically, a larger number of subcarriers increases the overall FIM, thereby lowering the CRB as indicated by (34). Furthermore, this formulation establishes an intermediate relationship between

\mathbf{Q} and the localization CRB: given the user positions and frequency bands, the FIM is primarily determined by² \mathbf{Q} .

Further analysis reveals that the optimal analog design for maximizing different subcarrier components of FIMs varies, highlighting the significance of our work. By incorporating TTD units into the analog beamforming structure, frequency dependent phase control can be achieved, enabling more precise optimization of each FIMs component across subcarriers. This leads to a lower CRB and improved localization accuracy. Therefore, the number of TTDs is a critical factor influencing the localization performance of the proposed wideband near-field localization scheme, as an increase in the former will be beneficial for more flexible frequency independent phase control.

IV. ANALOG COMBINATION COEFFICIENT DESIGN

While the localization scenario considered in the previous section focused on fixed analog combining (which dictates the beampattern of the ELAA), we next utilize its formulation to jointly localize and analog combining design generated by the TTD-based ELAA. We thus formulate the optimization problem of analog coefficient design in Section IV-A. In Section IV-B, we optimize the phase of PSs for a fixed time delay configuration, then optimizing the time delay of TTDs for a fixed PSs configuration. Finally, in Section IV-C, we extend these designs to also carry out localization, via an iterative algorithm for joint optimization position estimation and analog coefficient design.

A. Problem Formulation

According to (6), the design of PSs and TTDs contribute to effective localization leveraging the hybrid array setup, where PSs are frequency independent while TTDs are frequency dependent. By optimizing the configurations of PSs and TTDs, the localization process can be enhanced, ultimately leading to improved accuracy and reliability in position estimation.

As discussed in Section III-C, we design \mathbf{Q} to maximize the average of the trace of FIM³, which is expressed as

$$\begin{aligned} &\max_{\{\mathbf{Q}_m\}_{m=1}^M} \text{tr}[\mathbf{F}] \\ &\text{s.t. (9), (7), (8),} \\ &\quad t_{i,l} \in [0, t_{\max}]. \end{aligned} \quad (35)$$

According to (28)-(32), by substituting the definition of \mathbf{Q} and removing the irrelevant variable, problem (35) can be rewritten as

$$\begin{aligned} &\max_{\{\mathbf{T}_m\}_{m=1}^M, \mathbf{A}} \sum_{m=1}^M \text{tr}[\mathbf{T}_m \mathbf{A} \mathbf{U}_m \mathbf{U}_m^H \mathbf{A}^H \mathbf{T}_m^H] \\ &\text{s.t. (9), (7), (8),} \\ &\quad t_{i,l} \in [0, t_{\max}]. \end{aligned} \quad (36)$$

Where $\mathbf{U}_m = \mathbf{D}_m + \mathbf{B}_m$. Given the structural constraints outlined in (7) and (8), Problem (36) is non-convex, primarily

²Although the FIM also depends on the symbol matrix \mathbf{C} as shown in (29)-(32), this work assumes no interaction between users and the base station, and thus treats pilot symbols as random variables without optimizing their design. However, in scenarios involving user-base station coordination, pilot optimization could further improve localization performance.

³The randomness inherent in pilot symbols results in variations in the FIM obtained from each sampling instance. Consequently, it is necessary to compute the statistical average to mitigate the effects of this variability.

due to the coupled nature of the optimization variables, i.e., \mathbf{T}_m and \mathbf{A} . To address this challenge, an alternate optimization strategy is employed to disentangle \mathbf{T}_m and \mathbf{A} . This iterative alternate approach continues until convergence is achieved, facilitating the optimization process in a computationally feasible manner to approximate the optimal solution.

B. Alternating Optimization for TTDs and PSs

1) *Phase design for given time delay*: For given \mathbf{T}_m , the constrains on $t_{i,l}$ and structure constraint (7) in problem (36) can be removed. Define $\mathbf{u}_{m,k}$ as the k -th column of \mathbf{U}_m and $\bar{\mathbf{a}} = \text{vec}(\mathbf{A}) \in \mathbb{C}^{N_d N \times 1}$. Then $\mathbf{T}_m \mathbf{A} \mathbf{u}_{m,k} = (\mathbf{u}_{m,k})^T \otimes \mathbf{T}_m \bar{\mathbf{a}}$. Define $\tilde{\mathbf{W}}_{m,k} = (\mathbf{u}_{m,k})^T \otimes \mathbf{T}_m$. We can then remove the structure constraint (8) in (36) and rewrite the problem as

$$\begin{aligned} \max_{\bar{\mathbf{a}}} \bar{\mathbf{a}}^H \left(\sum_{m=1}^M \sum_{k=1}^K \tilde{\mathbf{W}}_{m,k}^H \tilde{\mathbf{W}}_{m,k} \right) \bar{\mathbf{a}} \\ \text{s.t. (9)}. \end{aligned} \quad (37)$$

Given that the zero elements of $\bar{\mathbf{a}}$ does not impact the objective function of (37), (37) can be simplified as

$$\begin{aligned} \max_{\tilde{\mathbf{a}}} \tilde{\mathbf{a}}^H \left(\sum_{m=1}^M \sum_{k=1}^K \tilde{\tilde{\mathbf{W}}}_{m,k}^H \tilde{\tilde{\mathbf{W}}}_{m,k} \right) \tilde{\mathbf{a}} \\ \text{s.t. (9)}. \end{aligned} \quad (38)$$

where $\tilde{\mathbf{a}} = [a_1, \dots, a_N]^T \in \mathbb{C}^N$ is the modified version of $\bar{\mathbf{a}}$ obtained by removing all the zero elements of $\bar{\mathbf{a}}$, and $\tilde{\tilde{\mathbf{W}}}_{m,k}$ is the modified version of $\tilde{\mathbf{W}}_{m,k}$ by removing the elements having the same index as the zero elements of $\bar{\mathbf{a}}$.

According to the constraint (9), solving (38) can be viewed as a search process for \mathbf{R} with the searching space is a product of N complex circles, which is a Riemannian submanifold of \mathbb{C}^N . Consequently, addressing (38) can be accomplished using the Riemannian conjugate gradient (RCG) algorithm. Specifically, the solution to (38) is iteratively updated according to

$$[\tilde{\mathbf{a}}^{(p+1)}]_n = \frac{[\tilde{\mathbf{a}}^{(p)} + \epsilon^{(p)} \boldsymbol{\xi}^{(p)}]_n}{\|[\tilde{\mathbf{a}}^{(p)} + \epsilon^{(p)} \boldsymbol{\xi}^{(p)}]_n\|}, \forall n. \quad (39)$$

Here, $[\tilde{\mathbf{a}}^{(p+1)}]_n$ represents the updated point derived from the current point $[\tilde{\mathbf{a}}^{(p)}]_n$, with p indicating the iteration count.

The solution utilizing the RCG method can be seen as an enhancement over the projection-based approach. $\epsilon^{(p)}$ denotes the Armijo step size [25] in the p -th iteration, while $\boldsymbol{\xi}^{(p)}$ signifies the search direction at the point $\tilde{\mathbf{a}}^{(p)}$, lying within the tangent space of the complex circle manifold at that specific point. This direction is given by

$$\begin{aligned} w \boldsymbol{\xi}^{(p)} = -\text{grad } g(\tilde{\mathbf{a}}) + \\ \zeta^{(p)} \left(\boldsymbol{\xi}^{(p-1)} - \text{Re} \left(\boldsymbol{\xi}^{(p-1)} \circ \tilde{\mathbf{a}}^{(p)\dagger} \right) \circ \tilde{\mathbf{a}}^{(p)} \right), \end{aligned} \quad (40)$$

where \dagger and \circ signify conjugation and the Hadamard product respectively, $\zeta^{(p)}$ is selected as the Polak-Ribiere parameter [25]. $\text{grad } g(\tilde{\mathbf{a}})$ represents the Riemannian gradient of $g(\tilde{\mathbf{a}})$, computed as the orthogonal projection of the Euclidean gradient of $g(\tilde{\mathbf{a}})$, given by

$$\text{grad } g(\tilde{\mathbf{a}}) = \nabla g(\tilde{\mathbf{a}}) - \text{Re} \left(\nabla g(\tilde{\mathbf{a}}) \circ \tilde{\mathbf{a}}^{(p)\dagger} \right) \circ \tilde{\mathbf{a}}^{(p)}, \quad (41)$$

where $\nabla g(\tilde{\mathbf{a}})$ is the Euclidean gradient of $g(\tilde{\mathbf{a}})$, which is defined from (38) as

$$\nabla g(\tilde{\mathbf{a}}) = 2 \left(\sum_{m=1}^M \sum_{k=1}^K \tilde{\tilde{\mathbf{W}}}_{m,k}^H \tilde{\tilde{\mathbf{W}}}_{m,k} \right) \tilde{\mathbf{a}}. \quad (42)$$

With the given time delay setting of TTDs, we can compute $\{a_n\}_{n=1}^N$ iteratively with (39) to (42), then we consider to determine the time delay with a given phase of PSs.

2) *Time Delay Design for Given Phase*: For given \mathbf{A} , (36) reduces to

$$\begin{aligned} \max_{\{\mathbf{T}_m\}_{m=1}^M} \sum_{m=1}^M \text{tr} [\mathbf{T}_m \mathbf{A} \mathbf{U}_m \mathbf{U}_m^H \mathbf{A}^H \mathbf{T}_m^H] \\ \text{s.t. (7), } t_{i,l} \in [0, t_{\max}], \forall i, l. \end{aligned} \quad (43)$$

We define $\bar{\mathbf{v}}_m = \text{vec}(\mathbf{T}_m)$ and $\tilde{\mathbf{Z}}_{m,k} = (\mathbf{A} \mathbf{u}_{m,k})^T \otimes \mathbf{I}_{N_d}$ and rewrite (43) as

$$\begin{aligned} \max_{\tilde{\mathbf{v}}_m} \sum_{m=1}^M \tilde{\mathbf{v}}_m^H \left(\sum_{k=1}^K \tilde{\tilde{\mathbf{Z}}}_{m,k}^H \tilde{\tilde{\mathbf{Z}}}_{m,k} \right) \tilde{\mathbf{v}}_m \\ \text{s.t. } \tilde{\mathbf{v}}_m = [e^{-j2\pi f_m t_1}, \dots, e^{-j2\pi f_m t_{N_d}}]^T, \\ t_{i,l} \in [0, t_{\max}], \forall i, l. \end{aligned} \quad (44)$$

Here $\tilde{\mathbf{v}}_m$ is the modified version of $\bar{\mathbf{v}}_m$, and $\tilde{\tilde{\mathbf{Z}}}_{m,k}$ is the modified version of $\tilde{\mathbf{Z}}_{m,k}$ by removing the elements having the same index as the zero elements of $\bar{\mathbf{v}}_m$. Problem (44) can be characterized as $N_d N_t$ single-variable optimization problem concerning $t_{i,l}$. Although deriving a closed-form solution for (44) is complex, the problem can be effectively addressed using numerical techniques like iterative one-dimensional search methods for practical computation. Specifically, define a searching set $\mathcal{S} = \{0, t_{\max}/Q, 2t_{\max}/Q, \dots, t_{\max}\}$, where Q is the sample number. In each iteration, each $t_{i,l}$ is updated by one-dimensional searching in \mathcal{S} .

C. Alternating Localization and Array Coefficient Design

The analog design method previously discussed relies on location information that may not be readily accessible in practical scenarios. Nonetheless, drawing inspiration from [37], an efficient alternating optimization approach can be employed for joint analog domain design and localization. Specifically, [46] reveals that even when the focus position at the receiving array deviates from the actual source position, improvements in the estimated results are observed. This enhancement persists despite discrepancies between the focus position and the user's true location, with the focus gain being present but attenuated. This suggests that once an initial estimation of the source location is acquired, iterative refinement towards the genuine source position is achievable by updating the focus position. Simultaneously, the adjustment of \mathbf{Q}_m can be synchronized with the iterations in the AP algorithm. In essence, an alternating algorithm can be devised by integrating the update of \mathbf{Q}_m into Algorithm 1, which is summarized as Algorithm 2.

In Algorithm 2, we utilize the receiving vector derived from random coefficient responses to initialize the position estimation. Subsequently, we update the coefficients of \mathbf{Q}_m based on the outcomes of the preceding position estimation to obtain new

Algorithm 2 Alternating localization and beamfocusing

Initialize: Initialize the matrix $\{\mathbf{Q}_m^1\}_{m=1}^M$ by the definition with random PSs setting \mathbf{A}^1 and TTDs setting \mathbf{T}_m^1 which satisfies $t_{i,l} \in [0, t_{\max}]$; $t = 1$; Iterations limit K_t . Obtain the initial position estimation as $(\mathbf{d}^1, \boldsymbol{\theta}^1)$ by Algorithm 1 (Steps 1-4).

While $t \leq K_t$ **do**

For $m = 1 : M$

- 1: Estimate (d_k^t, θ_k^t) by maximizing (19) with given \mathbf{Q}_m^t .
- 2: Update position set: $[\mathbf{d}]_k = d_k^t$.

End

3: Update \mathbf{A}^t via solving (37) with $\mathbf{T}_m = \mathbf{T}_m^t, \forall m$.

4: Update \mathbf{T}_m^t via solving (43) with $\mathbf{A} = \mathbf{A}^t$.

5: Update receive vector \mathbf{y}^{t+1} from \mathbf{Q}_m^{t+1} by (13).

6: $t = t + 1$

End while

Output: The position estimation $(\mathbf{d}, \boldsymbol{\theta}) = (\mathbf{d}^{K_t}, \boldsymbol{\theta}^{K_t})$.

observations. Different from the alternating algorithm in [37], in this paper the coefficient update is targeted at the wideband multi carrier scenarios, which require setting analog coefficients for multiple subcarriers separately, and the relevant design methods have been discussed in Section IV-B. This iterative procedure, repeated at each receiving time slot, enables a step-by-step convergence of the estimated result towards the true source location.

V. NUMERICAL EVALUATIONS

A. Simulation Parameters

In this section, we provide numerical results to demonstrate the efficiency of proposed localization algorithm and analog coefficients design scheme. In our experiments, the receiver array is set at configured as line array lying on the Y-axis with the array's reference position situated at $(0, 0)$ m, to positioning two users in X-Y plane, i.e., $K = 2$. In this case, the position of two users is set as $(8 \text{ m}, \pi/3)$ and $(8 \text{ m}, \pi/4)$ in polar coordinates, respectively. For convenience, the noise variance σ_m^2 is set to adjust SNR of each sub-carrier at antennas as a unified value, i.e., $\text{SNR} = 10\log(\|\mathbf{x}_m\|^2 / (N\sigma_m^2))$, $\forall m$. Furthermore, the other basic simulation parameters are given in Table I, which is exploited throughout our simulations unless otherwise specified.

The numerical indicators of localization performance are represented by the root mean square error (RMSE), calculated as

$$\text{RMSE} = \frac{1}{K} \sum_{k=1}^K \sqrt{\frac{1}{N_c} \sum_{n_c=1}^{N_c} e_{k,n_c}^2}, \quad (45)$$

where N_c is the number of Monte Carlo iterations, $e_{k,n_c}^2 = |(\mathbf{x}_k, \mathbf{y}_k) - (\hat{\mathbf{x}}_k^{(n_c)}, \hat{\mathbf{y}}_k^{(n_c)})|^2$ is the squared localization error (i.e., the distortion) of the k -th user, $(\hat{\mathbf{x}}_k^{(n_c)}, \hat{\mathbf{y}}_k^{(n_c)})$ are the estimated coordinates at the n_c -th Monte Carlo simulation.

B. Numerical Results

We first demonstrate that the design of \mathbf{Q} realizes a form of beam focusing, for this purpose, a heatmap is provided in Fig. 2. Specifically, we consider a $20 \times 20, \text{m}^2$ area with a resolution of 0.1 meters, where the antenna array is positioned at the origin. One user traverses all grid points and stays at each grid point for a positioning cycle to transmit pilot signals,

TABLE I
EXPERIMENT PARAMETERS

Parameter	Value
Central frequency	$f_c = 300 \text{ GHz}$
Bandwidth	$B = 30 \text{ GHz}$
Subcarrier number	$M = 12$
Sample number	$L = 256$
Array antenna number	$N = 256$
RF chain number	$N_d = 8$
TTD number per RF chain	$N_t = 16$
Antenna spacing	$\Delta = 5 \times 10^{-4} \text{ m}$
The maximum time delay	$t_{\max} = 5 \text{ ns}$
Near-field distance	$d_F = 32.5 \text{ m}$

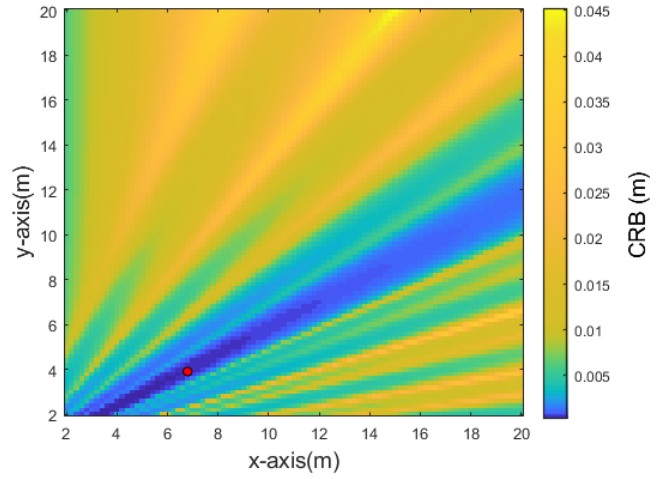


Fig. 2. The heatmap for the CRB on user position estimate by varying user positions, SNR is fixed as -10 dB. The magenta square denotes the array position. The red point is the predetermined position that analog design focuses on.

while \mathbf{Q} is designed to focus on the predetermined focal point as shown in Fig. 2 (i.e., \mathbf{Q} is derived by solving problem (36) based on the FIMs corresponding to the fixed focal point). The array then localizes the user using the actual received pilot signal with this fixed \mathbf{Q} in each positioning cycle. As illustrated in Fig. 2, the CRB for localization estimation is significantly reduced only when the user's true position is near the focal point of \mathbf{Q} . This observation confirms the relationship between the proposed simulated beamforming design and the actual user position, thereby validating our claim that \mathbf{Q} realizes a form of beam focusing in near field wideband localization.

Then, to demonstrate the effectiveness of the proposed localization algorithm, we provide one localization track map in the Monte Carlo simulation, as shown in Fig. 3. In Algorithm 1, localization is performed under a given \mathbf{Q} , though this setup is not realistic in practice since the true user position is unknown, we assume that \mathbf{Q} is perfectly designed to ensure a fair comparison with Algorithm 2. By contrast, Algorithm 2 alternates between localization and \mathbf{Q} design in an iterative manner. As observed, the estimated position trajectories of both algorithms gradually converge from the initial estimate toward

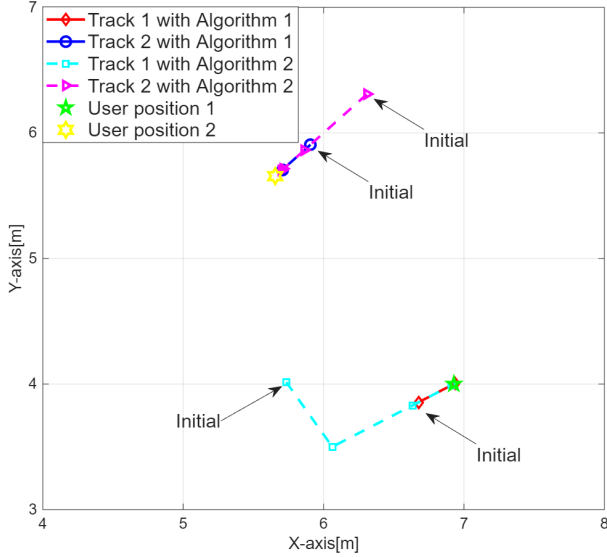


Fig. 3. Position estimations track map for each iteration of Algorithm 1 and Algorithm 2 with SNR $\text{SNR} = -10$ dB.

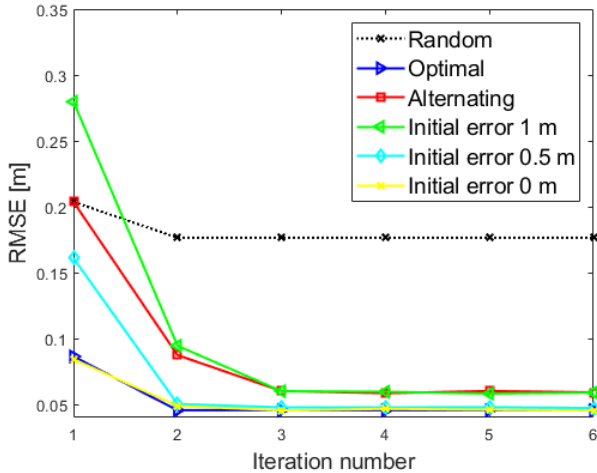


Fig. 4. Contrast of the number of iterations required for convergence via multiple contrast schemes with SNR $\text{SNR} = -5$ dB.

the true user position as iterations proceed. Moreover, it is worth noting that Algorithm 1 achieves a more accurate initial position estimate compared to Algorithm 2 and converges faster to the true position. This clearly highlights the impact of \mathbf{Q} design on the overall localization performance.

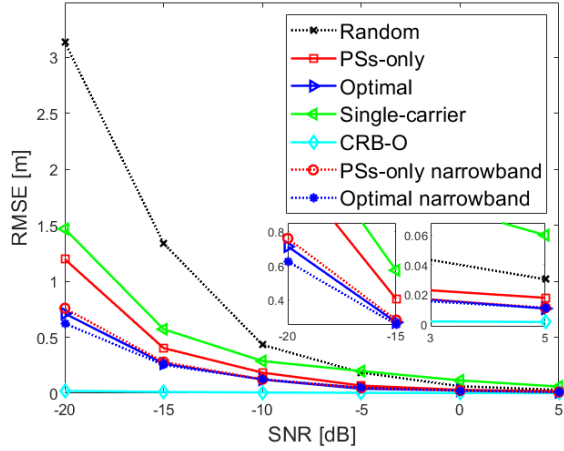
To evaluate the efficacy of the analog coefficient design in the joint localization and beamfocusing algorithm, we initially explored the convergence behavior of Algorithm 2, as illustrated in Fig. 4. Here, the curve “Alternating” refers to localization using the proposed Algorithm 2 with a random analog coefficient set as initial. For comparative analysis, we established three contrasting schemes with different initial error as 0 m, 0.5 m and 1 m. Specifically, in above contrast schemes, we still localization with Algorithm 2, but assume that we have an indistinct pre knowledge of users locations, where the location

error is a Gaussian-distributed random variable centered on the corresponding setting standard deviation, the initial analog coefficient \mathbf{Q}_m^1 in Algorithm 2 is obtained by solving (37) and (43) with such initial locations. The extreme schemes are also provided, involve localization via Algorithm 1 with predetermined analog setting. In such schemes, “Random” indicates that \mathbf{A} and \mathbf{T}_m are randomly set within specific constraints, while “Optimal” signifies that \mathbf{A} and \mathbf{T}_m are iteratively optimized by solving (37) and (43) with the perfect knowledge of users locations.

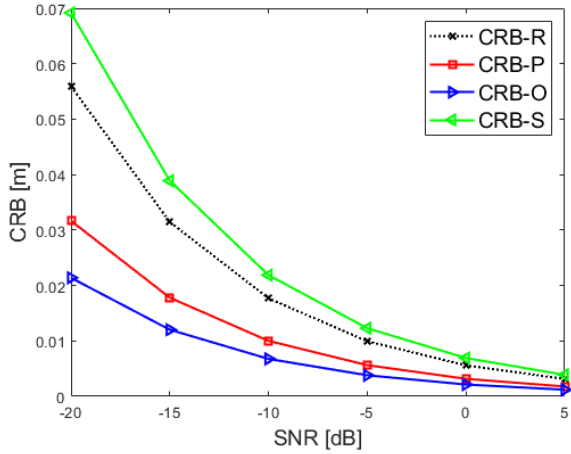
In Fig. 4, it is evident from the results that the RMSE of the proposed alternate scheme gradually converges from the level of the random scheme towards close to that of the optimal scheme, while the deviation of the convergence result depends on the initial error. Once the initial error is small enough, e.g., 0.5 m, it can achieve the almost same performance as the optimal scheme which has the perfect knowledge of users locations. Although the alternate scheme generally necessitates more iterations for convergence compared to the optimal scheme, this is attributed not only to the initial position estimation but also to the additional updates for the analog design. Nonetheless, the iteration process for analog design proves to be efficient, by iteratively analog coefficient design through Algorithm 2, the localization accuracy has been improved from decimeter level to centimeter level.

We illustrate the effectiveness of the analog design scheme we proposed in Fig. 5, displaying the RMSE of location estimation across various schemes under varying SNRs. As previously discussed, the analog design scheme attains optimal performance when the position information is known. Therefore, we utilize the aforementioned optimal scheme as a benchmark for performance comparison and calculate the CRB under this optimal scenario denoted as “CRB-O”. To showcase the performance enhancement derived from the analog design and further highlight the performance gains resulting from the incorporation of a time delay device, we include the random scheme and the PSSs-only scheme for comparison, above analog coefficients of schemes are design randomly, and derived by solving (36) with $t_{\max} = 0$, serving as an additional reference point in the analysis, respectively. Additional, the single-carrier scheme is also provided to show the performance improvement from the multi-carriers introduction, where the single-carrier scheme is obtained from [37] by set $M = 1$. Finally, to evaluate the impact of the bandwidth to optimal scheme and phase-only scheme, we consider a narrowband case, i.e., “Optimal 2” and “Phase-only 2”, in such case, the the bandwidth is set as 300 MHz.

In Fig. 5(a), it is evident that the random scheme exhibits the highest RMSE compared to the other schemes in low SNR scenarios. Through the analog design achieved by solving (36), a substantial enhancement in RMSE is observed. Besides, it can be seen that the PSSs-only scheme would close to the optimal scheme in the narrowband case, since the beam split effect could be ignored in such case. Then in the wideband case, scenarios characterized by high SNRs, the proposed optimal localization scheme closely approaches the performance level of the CRB in comparison to the PSSs-only scheme. While in low SNR environments, the former demonstrates around 40% of the performance enhancement achieved by the latter, it indicates the necessity of the introduction of TTDs for the wideband system. An intriguing observation in the single-carrier scheme is that



(a) RMSE versus different SNR.



(b) CRB versus different SNR.

Fig. 5. RMSE contrast of multiple contrast schemes under different SNR with array setting. (a) RMSE-SNR; (b) CRB-SNR

while it exhibited the worst performance in high SNR scenarios, at low SNR levels, its focus obtained through analog design nearly matched the performance of the PSs-only scheme. This further indicates that the PSs network did not fully exploit the benefits of multi-carrier systems in wideband scenarios, underscoring the importance of incorporating TTDs in multi-carrier settings. To elucidate the outcomes depicted in Fig. 5(a), we present the CRB results from various schemes in Fig. 5(b). Here, “CRB-R”, “CRB-P” and “CRB-S” are computed using (34) with analog design derived from the random scheme, the phase-only scheme and the single-carrier scheme, respectively, under the bandwidth B_1 . The comparison of these CRB values mirrors the trends observed in the RMSE performance of their corresponding schemes, suggesting that the performance enhancement exhibited by the proposed scheme stems from its optimization of the CRB.

In Fig. 6, we observe the influence of the number of TTDs connected to each RF chain, denoted as N_t , on the localization efficiency. To ensure a fair comparison, we adjust the number of PSs connected to each TTD, denoted as N_s , in accordance with the variation of N_t to maintain the condition $N = N_d N_t N_s$ as specified in Table I, that the upper limit of N_t is $N_t = N/N_d$

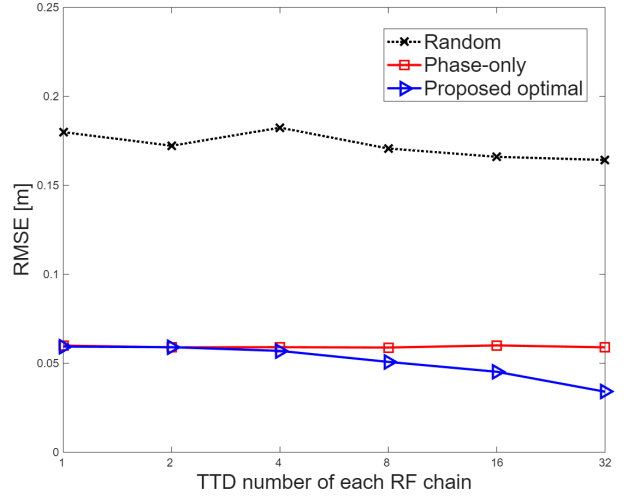


Fig. 6. RMSE contrast of multiple contrast schemes under different TTDs number of each RF chain with SNR = -5 dB.

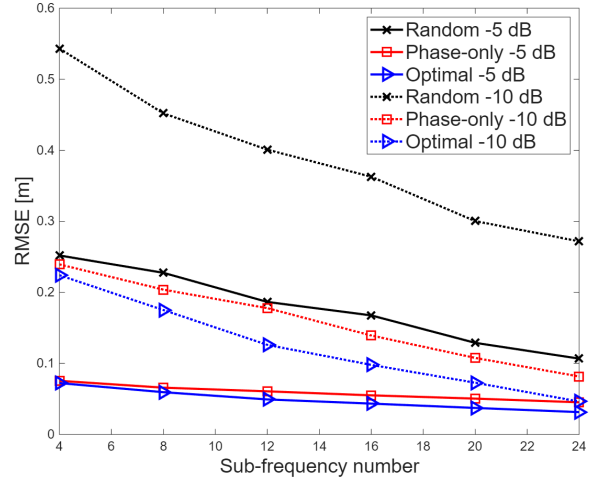


Fig. 7. RMSE contrast of multiple contrast schemes under different subcarrier number with SNR = -5 or -10 dB.

with $N_s = 1$. The proposed optimal scheme demonstrates improved performance with increasing N_t . This enhancement is attributed to the increased processing flexibility across multiple sub-carriers facilitated by the addition of more TTDs, thereby decelerate the beam splitting effect. In contrast, the performance of the random scheme and the phase-only scheme remains unaffected by changes in N_t . However, this performance enhancement is not as pronounced when N_t is less than the number of sub-carriers M . In such instances, the performance of the proposed optimal scheme tends to approach that of the phase-only scheme. Conversely, when the number of TTDs is maximized (i.e., one TTD per antenna), the localization performance exhibits the most substantial improvement. However, deploying a dedicated TTD for each antenna in an ELAA system may be impractical due to prohibitive cost considerations.

To further elucidate the impact of the relationship between the number of sub-carriers and the number of TTDs connected to

each RF chain on the performance of the proposed localization scheme, we present Fig. 7 showcasing the RMSE variations across different sub-carrier numbers. The results reveal that the performance of all schemes improves as the number of sub-carriers increases. This improvement can be attributed to the availability of more received information, a concept supported by the definitions of the FIMs derived in (29)-(32). Furthermore, it is evident that in scenarios with a small number of sub-carriers, the phase-only scheme closely matches the performance of the proposed optimal scheme. However, as the number of sub-carriers grows, a performance gap emerges between the two schemes, particularly when the number of sub-carriers exceeds N_t . This observation underscores that the primary advantage of integrating TTDs lies in resolving the limitation of PSs network in accurately processing multiple sub-carrier signals due to their frequency independence. The effectiveness of TTDs in managing multiple sub-carriers is contingent upon their quantity. A substantial performance enhancement necessitates a greater number of TTDs connected to each RF chain than the number of sub-carriers.

VI. CONCLUSIONS

In this work, our focus delved into wideband near-field multi-user localization utilizing a TTDs-based hybrid array. Initially, we elucidated the models pertaining to radiating near-field position estimation systems within the specified antenna architecture. Subsequently, we derived the CRB for the proposed estimation systems, and accordingly delineated the optimization strategy for the adjustable coefficients of the hybrid array to enhance position estimation accuracy, and introduced an efficient algorithm for simultaneous position estimation and adjustable coefficients design. The numerical outcomes underscored that the meticulous design of analog coefficients within the hybrid array wielded a substantial impact on enhancing near-field multi-source localization performance. Furthermore, the incorporation of TTDs was observed to improve the processing capabilities of the array, particularly in scenarios involving multi-carrier signals.

REFERENCES

- [1] H. Zhang *et al.*, "6G wireless communications: From far-field beam steering to near-field beam focusing," *IEEE Commun. Mag.*, vol. 61, no. 4, pp. 72–77, 2023.
- [2] M. Lotti *et al.*, "Radio SLAM for 6G systems at THz frequencies: Design and experimental validation," *IEEE J. Sel. Topics Signal Process.*, vol. 17, no. 4, pp. 834–849, 2023.
- [3] H. Chen *et al.*, "A tutorial on terahertz-band localization for 6G communication systems," *IEEE Commun. Surveys Tuts.*, vol. 24, no. 3, pp. 1780–1815, 2022.
- [4] H. Sarrifeddeen *et al.*, "Next generation terahertz communications: A rendezvous of sensing, imaging, and localization," *IEEE Commun. Mag.*, vol. 58, no. 5, pp. 69–75, 2020.
- [5] J. M. Jornet *et al.*, "The evolution of applications, hardware design, and channel modeling for terahertz (THz) band communications and sensing: Ready for 6G?" *Proc. IEEE*, pp. 1–32, 2024.
- [6] P. Zhang *et al.*, "Channel parameter estimation and localization for near-field XL-MIMO communications," *IEEE Trans. Veh. Technol.*, vol. 74, no. 9, pp. 14 781–14 786, 2025.
- [7] V. Petrov, J. M. Jornet, and A. Singh, "Near-field 6G networks: Why mobile terahertz communications MUST operate in the near field," in *Proc. IEEE Global Commun. Conf. (GLOBECOM)*, 2023, pp. 3983–3989.
- [8] I. Ahmed *et al.*, "A survey on hybrid beamforming techniques in 5G: Architecture and system model perspectives," *IEEE Commun. Surveys Tuts.*, vol. 20, no. 4, pp. 3060–3097, 2018.
- [9] R. Méndez-Rial *et al.*, "Hybrid MIMO architectures for millimeter wave communications: Phase shifters or switches?" *IEEE Access*, vol. 4, pp. 247–267, 2016.
- [10] N. Shlezinger *et al.*, "Artificial intelligence-empowered hybrid multiple-input/multiple-output beamforming: Learning to optimize for high-throughput scalable mimo," *IEEE Veh. Technol. Mag.*, vol. 19, no. 3, pp. 58–67, 2024.
- [11] Z. Ebadi *et al.*, "Near-field localization with antenna arrays in the presence of direction-dependent mutual coupling," *IEEE Trans. Veh. Technol.*, vol. 74, no. 5, pp. 7033–7048, 2025.
- [12] S. S. Ioushua and Y. C. Eldar, "A family of hybrid analog–digital beamforming methods for massive MIMO systems," *IEEE Trans. Signal Process.*, vol. 67, no. 12, pp. 3243–3257, 2019.
- [13] O. Lavi and N. Shlezinger, "Learn to rapidly and robustly optimize hybrid precoding," *IEEE Trans. Commun.*, vol. 71, no. 10, pp. 5814–5830, 2023.
- [14] O. Levy and N. Shlezinger, "Rapid and power-aware learned optimization for modular receive beamforming," *IEEE Trans. Commun.*, 2025, early access.
- [15] A. M. Elbir *et al.*, "Terahertz-band channel and beam split estimation via array perturbation model," *IEEE Open J. Commun. Soc.*, vol. 4, pp. 892–907, 2023.
- [16] M. Han *et al.*, "Tensor-based joint symbol detection, user localization and tracking for THz systems with dual-wideband effects," *IEEE Trans. Veh. Technol.*, vol. 73, no. 11, pp. 17 794–17 799, 2024.
- [17] Y. Chen *et al.*, "Hybrid precoding for wideband millimeter wave MIMO systems in the face of beam squint," *IEEE Trans. Wireless Commun.*, vol. 20, no. 3, pp. 1847–1860, 2021.
- [18] A. M. Elbir *et al.*, "The curse of beam-squint in ISAC: Causes, implications, and mitigation strategies," *arXiv preprint arXiv:2406.03162*, 2024.
- [19] L. Dai *et al.*, "Delay-phase precoding for wideband THz massive MIMO," *IEEE Trans. Wireless Commun.*, vol. 21, no. 9, pp. 7271–7286, 2022.
- [20] M. Cui and L. Dai, "Near-field wideband beamforming for extremely large antenna arrays," *IEEE Trans. Wireless Commun.*, vol. 23, no. 10, pp. 13 110–13 124, 2024.
- [21] Z. Wang *et al.*, "TTD configurations for near-field beamforming: Parallel, serial, or hybrid?" *IEEE Trans. Commun.*, vol. 72, no. 6, pp. 3783–3799, 2024.
- [22] Z. Wang, X. Mu, and Y. Liu, "Beamfocusing optimization for near-field wideband multi-user communications," *IEEE Trans. Commun.*, vol. 73, no. 1, pp. 555–572, 2025.
- [23] S. Aghashahi *et al.*, "Single antenna tracking and localization of ris-enabled vehicular users," *IEEE Trans. Veh. Technol.*, vol. 74, no. 3, pp. 4362–4375, 2025.
- [24] M. K. Ercan *et al.*, "RIS-aided NLoS monostatic multi-target sensing under angle-doppler coupling," *IEEE Trans. Veh. Technol.*, pp. 1–16, 2025.
- [25] H. Zhang *et al.*, "Beam focusing for near-field multi-user MIMO communications," *IEEE Trans. Wireless Commun.*, vol. 21, no. 9, pp. 7476–7490, 2022.
- [26] F. Guidi and D. Dardari, "Radio positioning with EM processing of the spherical wavefront," *IEEE Trans. Wireless Commun.*, vol. 20, no. 6, pp. 3571–3586, 2021.
- [27] Z. Abu-Shaban *et al.*, "Near-field localization with a reconfigurable intelligent surface acting as lens," in *Proc. IEEE Int. Conf. on Commun. (ICC)*, 2021, pp. 1–6.
- [28] A. Elzanaty *et al.*, "Towards 6G holographic localization: Enabling technologies and perspectives," *IEEE Internet Things Mag.*, vol. 3, no. 6, pp. 138–143, 2023.
- [29] C. Ozturk *et al.*, "RIS-aided near-field localization under phase-dependent amplitude variations," *IEEE Trans. Wireless Commun.*, vol. 22, no. 8, pp. 5550–5566, 2023.
- [30] Z. Wang *et al.*, "Near-field localization and sensing with large-aperture arrays: From signal modeling to processing," *arXiv preprint arXiv:2406.10941*, 2024.
- [31] D. Dardari *et al.*, "LOS/NLOS near-field localization with a large reconfigurable intelligent surface," *IEEE Trans. Wireless Commun.*, vol. 21, no. 6, pp. 4282–4294, 2022.
- [32] A. Gast, L. Le Magoarou, and N. Shlezinger, "DCD-MUSIC: Deep-learning-aided cascaded differentiable MUSIC algorithm for near-field localization of multiple sources," in *Proc. IEEE Int. Conf. Acoust. Speech Signal Process. (ICASSP)*, 2025.
- [33] A. A. D'Amico *et al.*, "Cramr-Rao bounds for holographic positioning," *IEEE Trans. Signal Process.*, vol. 70, pp. 5518–5532, 2022.
- [34] A. Elzanaty *et al.*, "Reconfigurable intelligent surfaces for localization: Position and orientation error bounds," *IEEE Trans. Signal Process.*, vol. 69, pp. 5386–5402, 2021.
- [35] A. Guerra *et al.*, "Near-field tracking with large antenna arrays: Fundamental limits and practical algorithms," *IEEE Trans. Signal Process.*, vol. 69, pp. 5723–5738, 2021.

- [36] Q. Yang *et al.*, “Near-field localization with dynamic metasurface antennas,” in *Proc. IEEE Int. Conf. Acoust. Speech Signal Process. (ICASSP)*, 2023.
- [37] —, “Beam focusing for near-field multi-user localization,” *IEEE Trans. Veh. Technol.*, vol. 74, no. 8, pp. 12 259–12 273, 2025.
- [38] N. T. Nguyen *et al.*, “Joint communications and sensing hybrid beamforming design via deep unfolding,” *IEEE J. Sel. Topics Signal Process.*, vol. 18, no. 5, pp. 901–916, 2024.
- [39] Z. Cai *et al.*, “Low-power beamforming design for near-field integrated sensing and communication networks,” *IEEE Internet Things J.*, 2025, early access.
- [40] X. Wang *et al.*, “Wideband near-field integrated sensing and communication with sparse transceiver design,” *IEEE J. Sel. Topics Signal Process.*, vol. 18, no. 4, pp. 662–677, 2024.
- [41] A. M. Elbir, K. V. Mishra, and S. Chatzinotas, “Spherical wavefront near-field DoA estimation in THz automotive radar,” in *Proc. European Conf. Antennas Propag. (EuCAP)*, 2024.
- [42] E. Bjornson, O. T. Demir, and L. Sanguinetti, “A primer on near-field beamforming for arrays and reconfigurable intelligent surfaces,” in *Proc. Asilomar Conf. Signals Syst. Comput.*, 2021, pp. 105–112.
- [43] Y.-D. Huang and M. Barkat, “Near-field multiple source localization by passive sensor array,” *IEEE Trans. Antennas Propag.*, vol. 39, no. 7, pp. 968–975, 1991.
- [44] H. L. Trees, *Classical Detection and Estimation Theory*. Hoboken, NJ, USA: Wiley, 2002.
- [45] R. Zhang, B. Shim, and W. Wu, “Direction-of-arrival estimation for large antenna arrays with hybrid analog and digital architectures,” *IEEE Trans. Signal Process.*, vol. 70, pp. 72–88, 2021.
- [46] P. Gavriilidis and G. C. Alexandropoulos, “Near-field beam tracking with extremely large dynamic metasurface antennas,” *IEEE Trans. Wireless Commun.*, vol. 24, no. 7, pp. 6257–6272, 2025.